A&A 367, 705–718 (2001)
DOI: 10.1051/0004-6361:20000455

Astronomy & Astrophysics

Parametric decay of circularly polarized Alfvén waves: Multidimensional simulations in periodic and open domains

L. Del Zanna[1], M. Velli[1], and P. Londrillo[2]

[1] Università di Firenze, Dipartimento di Astronomia e Scienza dello Spazio, Largo E. Fermi 5, 50125 Firenze, Italy
[2] Osservatorio Astronomico di Bologna, Via Ranzani 1, 40127 Bologna, Italy

Received 29 September 2000 / Accepted 5 December 2000

Abstract. The nonlinear evolution of monochromatic large-amplitude circularly polarized Alfvén waves subject to the decay instability is studied via numerical simulations in one, two, and three spatial dimensions. The asymptotic value of the cross helicity depends strongly on the plasma beta: in the low beta case multiple decays are observed, with about half of the energy being transferred to waves propagating in the opposite direction at lower wave numbers, for each saturation step. Correspondingly, the other half of the total transverse energy (kinetic and magnetic) goes into energy carried by the daughter compressive waves and to the associated shock heating. In higher beta conditions we find instead that the cross helicity decreases monotonically with time towards zero, implying an asymptotic balance between inward and outward Alfvénic modes, a feature similar to the observed decrease with distance in the solar wind. Although the instability mainly takes place along the propagation direction, in the two and three-dimensional case a turbulent cascade occurs also transverse to the field. The asymptotic state of density fluctuations appears to be rather isotropic, whereas a slight preferential cascade in the transverse direction is seen in magnetic field spectra. Finally, parametric decay is shown to occur also in a non-periodic domain with open boundaries, when the mother wave is continuously injected from one side. In two and three dimensions a strong transverse filamentation is found at long times, reminiscent of density ray-like features observed in the extended solar corona and pressure-balanced structures found in solar wind data.

Key words. magnetohydrodynamics (MHD) – waves – instabilities – methods: numerical – Sun: corona – solar wind

1. Introduction

Alfvén waves, transverse incompressible modes propagating in a magnetized plasma, are well known *exact* (i.e. regardless of their amplitude) solutions of the ideal compressible MHD equations, provided the overall magnetic field intensity is uniform. This particular property, makes such waves the natural candidates for energy transfer over large distances throughout a magnetized plasma.

In the heliospheric medium, Alfvén waves are preferentially observed in high-speed regions of the solar wind (Belcher & Davis 1971; Goldstein et al. 1995), where an outward propagating flux, of coronal if not photospheric origin, dominates the low frequency part of the fluctuation spectra. However, such modes are seen to evolve with distance from the Sun: the spectrum steepens and the prevalence of outward propagating modes, as measured by the (reduced) cross helicity σ, see Eq. (3), decreases monotonically (Roberts et al. 1987; Bavassano et al. 2000). This process is difficult to explain in terms of incompressible fluctuations, since in presence of an imbalance between outward and inward propagating modes, nonlinear coupling should increase the imbalance, thus leading to an ever purer outwardly propagating Alfvén mode (Dobrowolny et al. 1980). Several ways to stop this dynamical alignment effect have been proposed (interaction with transverse large scale magnetic field and velocity shears: Roberts et al. 1987; Malara et al. 1992; effects of the overall solar wind expansion, Zhou & Matthaeus 1989; Grappin & Velli 1996), but there is one very relevant process which has yet to be fully investigated, namely parametric decay.

When compressible motions are allowed in a plasma, circularly polarized Alfvén waves in parallel propagation, which have constant magnetic pressure, prove to be unstable solutions: the waves couple to density and other compressive fluctuations present in the plasma, leading to nonlinear wave steepening and shock dissipation, that disrupts the initially coherent states, generating a spectrum of magneto-acoustic and Alfvén modes propagating both parallel and anti-parallel to the initial direction. Finally energy cascades in all directions available. This process

Send offprint requests to: L. Del Zanna,
e-mail: ldz@arcetri.astro.it

has been invoked in phenomenological models of the evolution of turbulence in the solar wind, as the mechanism responsible for the generation of the incoming waves necessary to evolve the spectra, as in Schmidt & Marsch (1995) and sequels, but a quantitative study of the process is still lacking, especially concerning full 3-D MHD simulations.

In the solar corona the same mechanism could help to solve the longstanding problem of triggering an MHD turbulent cascade towards the small scales needed for dissipation and heating, since in spite of the smallness of the local wave amplitudes, the low-β plasma should make the instability time-scales short enough to allow the production of backscattered Alfvénic modes and magnetosonic waves (subject to fast steepening and shock dissipation) at reasonably short coronal distances. For a general discussion of the role that Alfvén waves are likely to play when coupled to compressive modes in the coronal heating scenario, the reader is referred to Del Zanna & Velli (2000), where preliminary results of the present work are also given.

Parametric decay was first studied long ago: Galeev & Oraevsky (1963) and Sagdeev & Galeev (1969) considered the low beta limit for 1-D propagating modes. The general dispersion relation for the growing compressive mode was derived independently by Derby (1978) and Goldstein (1978), whose analysis was completed much later by Jayanti & Hollweg (1993). Dispersive effects were first included by Longtin & Sunnerup (1986) and by Wong & Goldstein (1986), while an overall analysis of all the different families of parametric instabilities in this approximation may be found in Hollweg (1994). The first study of the nonlinear development of the parametric instability, both through an analytic perturbation expansion and via numerical simulations, was carried out by Hoshino & Goldstein (1989), indicating the possibility of MHD turbulence as the outcome of the decay process. An initial incoherent spectrum of Alfvén waves was considered by Cohen & Dewar (1974) and Cohen (1975) in the quasilinear approximation, assuming strong Landau-damping of the sound waves. In this limit, they showed that spectra with power law indices steeper than -1 should be stable, while flatter spectra were found to be unstable. However direct numerical simulations by Umeki & Terasawa (1992) showed that, within the MHD framework, spectra of incoherent waves are always unstable regardless of the index of the power-law spectrum. In their simulations the initial spectrum of large-amplitude Alfvén waves was not in equilibrium, since the overall magnetic field magnitude was not constant. To investigate the instability of a spectrum of waves in detail, without having to deal with the compressible modes generated by the gradient of the magnetic pressure (the ponderomotive force), Malara & Velli (1996) focused on the decay of a spectrum with initial constant total field magnitude and showed how the growth rate decreases for a non-monochromatic mother wave. This study was extended up to the nonlinear saturation stage in Malara et al. (2000). A 2-D analysis was performed by Viñas & Goldstein (1991), and numerical simulations in 2-D were carried out by Ghosh et al. (1993), Ghosh & Goldstein (1994) and Ghosh et al. (1994). Their results show that parametric decay can occur also at oblique directions in the low beta case and that a new filamentation-like instability occurs at large angles in the high beta case. Finally, the periodic simulation box constraint was first relaxed by Pruneti & Velli (1997), who studied Alfvén waves propagating upwards in a gravitationally stratified medium with open boundaries, both in 1-D and 2-D: again, parametric decay was shown to occur though with some differences due to the non-periodicity of the simulation domain and to the (mild) stratification.

In this paper the decay of monochromatic large-amplitude Alfvén waves will be studied by means of a recently developed upwind 3D-MHD code, both in a periodic numerical domain and in conditions of open boundaries. Here we will restrict our study to circularly polarized waves in parallel propagation. The main reason for this choice is to extend previous 1-D works to 3-D and to have the condition of constant magnetic pressure automatically satisfied. In a forthcoming paper we will study the stability of the nonlinear extension of linearly polarized waves (arc-waves and spherically polarized waves, Barnes & Hollweg 1974; see also Grappin et al. 2000 and references therein), which represent more general cases observed in the fast solar wind. The goal of the present paper is threefold: first we study the long-term nonlinear development of parametric decay after saturation in one spatial dimension (1-D) under a wide range of plasma parameters; secondly we move to the 2-D and to full 3-D cases, analyzing the changes with respect to the one-dimensional results and studying the multidimensional spectra; finally we relax the restriction of periodic boundary conditions in the direction of the background magnetic field and we study the 2-D and 3-D decay of an Alfvén wave which is steadily injected from one of the two open sides.

The paper is organized as follows. In Sect. 2 we describe the wave initial conditions and parameters of our study. In Sect. 3 we briefly discuss the numerical technique used, which allows us to consider the development of turbulence even in the presence of shocks (generated by the unstable compressive modes) via a high order upwind-type algorithm. Section 4 is devoted to the 1-D results, both in low beta and intermediate beta regimes, while in Sect. 5 we present the 2-D and 3-D cases with emphasis on the modification induced by the higher dimensionality. The evolution of a wave injected from one side of a 3-D domain with open boundaries along the background field direction is considered in Sect. 6 while the results are summarized in Sect. 7.

2. Model parameters

The whole analysis will be performed in the framework of single-fluid ideal MHD, thus neglecting dispersive effects and explicit dissipative terms. The equations are solved in conservative form, employing an ideal energy equation

Table 1. Simulation parameters for the three runs, labeled A, B and C. The wave numbers k_c and $k_t^{\pm}$ are those expected to be excited, with a linear growth rate γ, from an inspection of Fig. 1

run	η	β	k_0	k_c	k_t^+	k_t^-	γ
A	0.2	0.1	4	6	10	2	0.41
B	0.5	0.5	4	5	9	1	0.39
C	1.0	1.2	4	5	9	1	0.41

($\gamma = 5/3$), while the induction equation for $\boldsymbol{B}$ is replaced by the corresponding equation for the magnetic vector potential $\boldsymbol{A} = \nabla \times \boldsymbol{B}$.

We consider an initial state characterized by a uniform magnetized plasma ($B_z = B_0$, $v_z = 0$, $\rho = \rho_0$, $p = p_0 = (\beta/\gamma)B_0^2$) plus a circularly polarized monochromatic Alfvén wave in parallel propagation with components in the orthogonal plane given by

$$B_x = \eta B_0 \cos(k_0 z), \quad B_y = \eta B_0 \sin(k_0 z), \tag{1}$$

and $\boldsymbol{v}_\perp = -\boldsymbol{B}_\perp/\sqrt{\rho_0}$. Here we have defined the plasma β as the squared ratio of the sound speed $c_s = \sqrt{\gamma p_0/\rho_0}$ to the Alfvén speed $v_A = B_0/\sqrt{\rho_0}$, η is the wave amplitude with respect to the background field B_0, while k_0 and $\omega_0 = v_A k_0$ are the wave number and frequency, respectively, of the mother wave. In the following we choose the normalization $\rho_0 = B_0 = 1$, so that $v_A = 1$ and $c_s = \sqrt{\beta}$. In order to trigger the instability, we perturb the background density with a point-wise random flat noise with a root mean square (rms) value of $\epsilon = 10^{-4}$. The noise depends on all spatial coordinates, thus allowing unstable wave propagation in the transverse directions too.

The linear growth of the 1-D parametric instability has been extensively studied in the literature. Briefly, the decay of the mother wave occurs via the resonant creation of a longitudinal compressive mode (with wave number k_c and frequency ω_c) and two sideband transverse modes ($k_t^{\pm} = k_c \pm k_0$, $\omega_t^{\pm} = \omega_c \pm \omega_0$). During the linear phase of the instability all these modes grow exponentially in time absorbing energy from the mother wave. Only in the small-amplitude and low-β ($\eta, \beta \ll 1$) limits the excited waves coincide with normal modes, that is a forward propagating sound wave ($\omega_c = \sqrt{\beta} k_c$) and two oppositely propagating Alfvén waves ($\omega_t^{\pm} = \pm k_t^{\pm}$), with the positive mode being negligible (decay instability). As was pointed out by Jayanti & Hollweg (1993), the nature of the parametric instability changes for $\beta \geq 1$, when the dominant unstable mode becomes the forward propagating transverse wave (beat instability).

The dispersion relation for the daughter waves for a generic β (Derby 1978; Goldstein 1978) may be written as

$$(\omega^2 - \beta k^2)(\omega^{+2} - k^{+2})(\omega^{-2} - k^{-2}) =$$

$$\eta^2 k^2 (\omega - k)(\omega^3 + k\omega^2 - 3\omega + k), \tag{2}$$

where we have normalized as usual $k/k_0 \to k$, $\omega/\omega_0 \to \omega$, $k^{\pm} = k \pm 1$, $\omega^{\pm} = \omega \pm 1$ (note that $\omega^{\pm 2} - k^{\pm 2} = (\omega - k)(\omega + k \pm 2)$). The solution of Eq. (2) is plotted in Fig. 1 for three different sets of parameters η and β, as listed in Table 1. The values have been chosen in order to simulate solar wind conditions, from the external corona outwards. With the present choice of parameters, the three predicted growth rates γ are very similar and so the characteristic time-scales will be comparable in all cases.

In our simulations, where the constraint of having integer wave numbers has to be taken into account when a periodic domain is employed (we use initially a multidimensional periodic box of size 2π, open boundaries will be introduced in Sect. 6 along the z direction) the value of $k_0 = 4$, which guarantees enough dynamics at larger wave numbers and allows inverse cascading for the values of the parameters η and β chosen, will be assumed throughout. In Table 1 we list the wave numbers of the modes expected to be excited and the corresponding growth rates (which are the same also for the $k^{\pm}$ modes and increase linearly with the order for higher sidebands, see Hoshino & Goldstein 1989), as derived from Fig. 1.

3. Numerical method

In the present work we use a recently developed finite differences *high order upwind* MHD code whose main features are here briefly summarized. For a more complete description we refer the reader to Londrillo & Del Zanna (2000) and to Londrillo et al. (2000). The code is specially designed to treat strong discontinuities, such as shocks or current sheets, as well as smoother features like waves or turbulent motion. To achieve this, up to fifth order ENO-like (Essentially Non-Oscillatory) interpolation polynomials are used. The upwind procedure is performed by a LLF (local Lax-Friedrichs) flux splitting, thus avoiding the time consuming decomposition into the characteristic modes, as is usual in many other (low order) upwind schemes. When equipped with a three-stage Runge-Kutta time integration procedure, the code achieves an overall fourth order (formal) accuracy in space and third order accuracy in time. Since upwind schemes integrate the MHD equations in ideal form, i.e. dissipative terms are not taken explicitly into account, high order is then an essential feature to keep the numerical viscosity (resistivity) low in smooth regions, still ensuring a proper description of flow discontinuities.

A second main feature of the present code relies on the way the MHD solenoidal constraint $\nabla \cdot \boldsymbol{B} = 0$ has been taken into account. This is a very important issue for upwind computations and has been subject of a vast debate in the last decade. Our recipe for treating the solenoidal constraint correctly is discussed in detail in Londrillo & Del Zanna (2000), here we just mention that $\nabla \cdot \boldsymbol{B} = 0$ can be cast in a conservation form only by placing the magnetic field components at cell interfaces, rather than at cell centers like the other fluid variables. Moreover, the magnetic components must be derived at each time step from the vector potential $\boldsymbol{A} = \nabla \times \boldsymbol{B}$ and its numerical

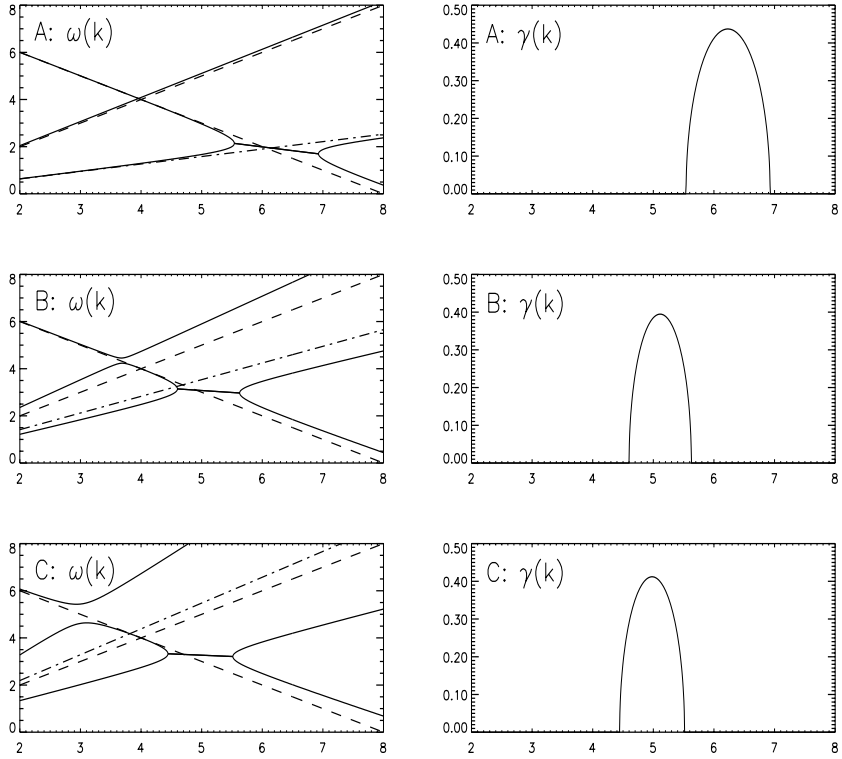

Fig. 1. Real and imaginary parts of the complex solutions of the dispersion relation Eq. (2), for the three runs in Table 1. On the left-hand side column we also plot the interacting normal modes in the $\eta \to 0$ limit, that is the two oppositely propagating Alfvén waves $\omega^{\pm} = \pm k^{\pm}$ (or $\omega = k$ and $\omega = 2 - k$, both indicated with a dashed line) and the sound wave $\omega = \sqrt{\beta} k$ (dot-dashed line). Note how far the unstable compressive mode can be from the normal mode when η is large. In run C the parametric process is actually a *beat* instability, where the positive transverse mode is more involved than the compressive one

flux $\boldsymbol{v} \times \boldsymbol{B}$ must be defined, along each component, by combined upwinding in the remaining two directions.

The present version of the MHD code is fully three-dimensional and has been parallelized along the third coordinate, by means of the *ghost cells* technique, with MPI parallel directives. For the largest simulations in the present work, a maximum of 32 processors have been employed (at least 4 grid points per processor are needed in the z direction). Different interpolation schemes, geometries and boundary conditions are supported, due to extensive use of modular structures in the code design. Of particular interest is the option for transparent *inflow/outflow* boundary conditions, which allows introduction of selected waves in the domain and transparent boundaries without spurious reflections, thanks to a field decomposition into characteristic modes (see the Appendix).

4. 1-D results

Before moving to the full 3-D case, we show some interesting results about the long-term nonlinear evolution of the parametric instability in one spatial dimension, in the three cases listed in Table 1. In this section we will always use a resolution of $N = 512$ grid points.

We find it useful to define the variables $\boldsymbol{z}^{\pm} = \delta\boldsymbol{v} \mp \delta\boldsymbol{B}/\sqrt{\rho}$, so that the initial state is characterized by the $\boldsymbol{z}^{+}$ component alone, with amplitude 2η and $\boldsymbol{z}^{-} = 0$. Note that the usual definition of the Elsässer variables $\boldsymbol{z}^{\pm}$ is different, in our notation the positive sign indicates propagation in the positive z direction. Other useful quantities are the spatially-averaged Elsässer energies and the normalized cross helicity, defined in our notation respectively by

$$E^{\pm} = < \frac{1}{2} |\boldsymbol{z}^{\pm}|^2 >, \quad \sigma = \frac{E^{+} - E^{-}}{E^{+} + E^{-}}, \tag{3}$$

where again the value of σ will be opposite than in the usual notation, so that here $\sigma = +1$ in the initial state of pure Alfvén waves propagating in the positive z direction.

In Fig. 2 we show the temporal evolution of σ and $E^{\pm}$, together with the exponential growth and subsequent saturation of two other quantities: the rms density fluctuations and a measure of the importance of compressive over transverse modes. The latter is defined through the ratio of the rms divergence and curl of the velocity field:

$$\zeta = \frac{\sqrt{< (\nabla \cdot \boldsymbol{v})^2 >}}{\sqrt{< |\nabla \times \boldsymbol{v}|^2 >}}. \tag{4}$$

The linear growth rates derived from the data match those predicted in Table 1 within an error less than 1%. The time histories of $\delta\rho_{\rm rms}$ and ζ look very similar and the linear growths are also clearly the same. The compressive modes reach the greatest amplitude when saturation occurs, corresponding with the maxima of both $\delta\rho_{\rm rms}$ and ζ.

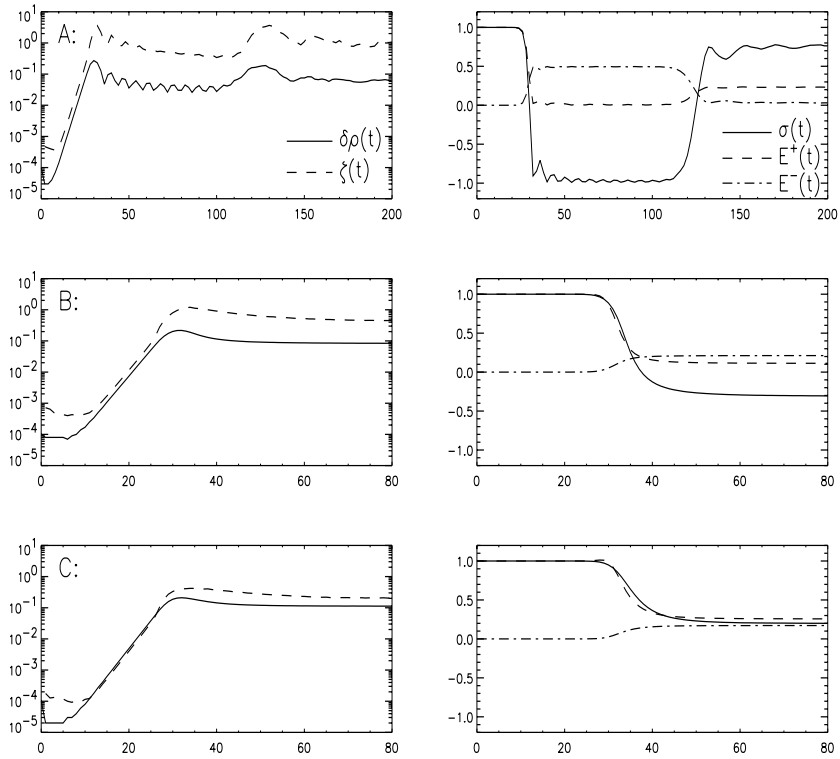

Fig. 2. Some rms quantities as a function of time for the usual three runs. On the left-hand side we plot in logarithmic scale the density fluctuations $\delta\rho_{\rm rms}$ (solid line) and the ζ function defined in the text (dashed line). The exponential growth and saturation phase are clearly recognizable. On the right-hand side we plot the normalized cross helicity (solid line) and the two Elsässer energies (dashed line for E^+, dot-dashed for E^-). Note the secondary instability occurring at time $t \simeq 130$ in run A. The sign of σ after the first instability strongly depends on the plasma β

From an inspection of the spatial profiles, it is apparent that the instability saturation always occurs when the density (or pressure) fluctuations and the longitudinal velocity have steepened into a train of shocks. We have also verified that these fluctuations are anti-correlated with corresponding steepened fluctuations in magnetic pressure, for all the three values of the plasma beta considered here. As an example of this situation, a snapshot for $t = 40$, well after the nonlinear saturation peak, is taken in Fig. 3 for runs A and C. Note the perfect correlation between δp and δv_z and the perfect anti-correlation between δp and δB^2 in both cases. The difference in scale is due to the mother wave amplitude, which in run C is five times larger than for run A; we may also notice that for $\beta < 1$ the kinetic pressure fluctuations dominates over the magnetic pressure fluctuations, whereas the opposite situation holds for $\beta > 1$.

Returning to Fig. 2, the right-hand side column displays the cross helicity and the Elsässer energies defined in Eq. (3) (the latter have been normalized against $E^+(0) = 2\eta^2$). At the time of nonlinear saturation the cross helicity drops together with E^+ while E^- grows in time, corresponding to the backscattered Alfvén wave with wave number $k_{\rm t}^-$. It is interesting to notice that both the decays of the cross helicity and of the total Alfvénic energy must be due to the presence of compressive modes and associated shock heating, since those quantities are conserved in an incompressible and ideal medium. For $\beta < 1$, the decay is so pronounced that σ reverses its sign, at saturation, implying that the energy in the backscattered daughter is now larger than that in the mother wave. From this point of view the most interesting case is clearly run A, where after saturation E^+ has dropped almost to zero ($\sigma = -1$) and half of the initial energy has gone to feed the backscattered wave (of the other half, 75% has gone into heat and 25% into energy carried by the sound wave). The situation is now almost the same as at the initial time, with a pure Alfvén mode propagating in a noisy density background. Since the new mother wave has a wave number greater than one ($k = 2$), we have decided to extend the simulation beyond $t = 80$ up to $t = 200$: the results show clearly a new occurrence of the decay instability with a behavior predictable from the usual linear theory with the new values of k_0 and η. At later times, after the secondary instability, the new dominant compressive mode has $k = 3$ while the dominant transverse mode has $k = 1$. We have also verified that this inverse cascade goes on when we start with a pump wave with $k_0 = 8$, reaching the final $k = 1$ value after three successive decay instabilities, this time with a negative asymptotic value for the cross helicity σ.

To our knowledge, this is the first time that multiple decay instabilities have been found in numerical simulations. We have investigated the conditions for the occurrence of such event, but it appears that it is not very easy to find the physical criteria for the multiple decay to

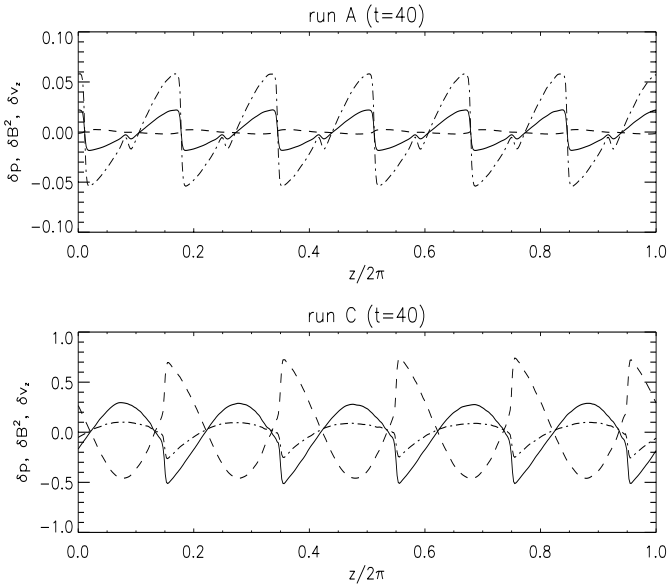

Fig. 3. Pressure (solid line), squared magnetic field strength (dashed line) and longitudinal velocity (dot-dashed line) fluctuations at $t = 40$, after nonlinear saturation, for runs A ($\beta < 1$) and C ($\beta > 1$). Shock waves always form, with the usual positive correlation between δp and v_z and an anti-correlation between δp and δB^2. In the low beta case we have larger pressure fluctuations, while in the high beta case we have larger magnetic fluctuations

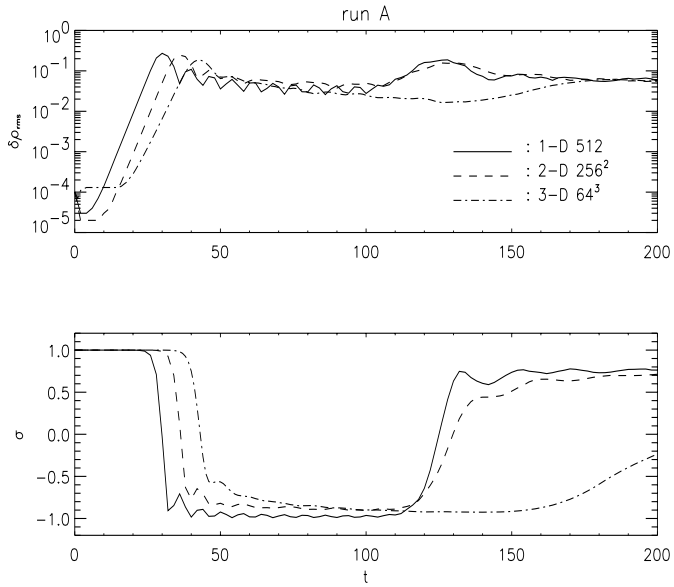

Fig. 4. Density fluctuations and cross helicity, for run A parameters, in the three cases 1-D, 2-D and 3-D. The 1-D macroscopic features are well maintained in higher dimensional simulations

occur. The strong decay of the mother wave, which is always found in the low-beta case, appears not to be a sufficient condition. At least three conditions must be satisfied:

1. the value of k_c must be far from the pump wave number k_0, so that the resulting k_t^- is large enough to allow new dynamics in wave number space, where only integers are allowed because of the periodic numerical box;
2. the linear instability range should be narrow, allowing just a few unstable wave numbers, so that the individual contributions do not mix together;
3. the level of the density fluctuations after saturation should be low, in order to reset a situation similar to that of the initial conditions, that is a large-amplitude transverse wave propagating in a noisy background.

To prove this, we have run six simulations with the same value $\beta = 0.1$ and different values of η: the density fluctuations were the lowest for the run A parameters ($\eta = 0.2$). For lower values the cross helicity showed still an oscillating behavior in the long-term evolution, but always stayed below zero and both Elsässer energies were very low after the second instability onset. On the other hand, increasing η, more modes are involved and the exchange of energy between the opposite traveling Alfvénic waves was less dramatic.

5. 2-D and 3-D results

When we move to higher dimensions, leaving the same initial conditions but introducing a point-wise random noise in the whole volume, so that a spatial dependence in the transverse directions is allowed, the time history of rms quantities looks remarkably similar to the evolution in the one-dimensional case. In the following discussion we will limit our analysis to run A, reducing the resolution to 256^2 grid points in 2-D and to 128^3 (and even to 64^3 for longer runs) in 3-D.

In Fig. 4 we plot the rms density fluctuations and cross helicity time histories for the 1, 2 and 3 dimensional cases: the primary and secondary decays occur also in 2-D and in 3-D though the time of their occurrence is slightly delayed in higher dimensions because the system has at disposal a higher number of degrees of freedom, thus the right unstable eigenmodes take longer to be selected. We have checked this point by running until $t = 40$ in 1, 2, and 3-D with the same resolution (128 grid points in each direction), confirming that the delay is not due to a higher numerical viscosity level. Clearly, the introduction of couplings transverse to the background magnetic field has little influence on the evolution of volume-averaged quantities. In particular the similar growth rates found in the different cases especially for the primary decay instability would seem to imply that the transverse couplings do not decrease the overall coherence of the daughter modes, or at least do not affect their stability properties. The secondary decay in 3-D occurs much later for the reason given above (but in this low resolution case we cannot exclude numerical effects too).

Examining the contours of different field profiles for the 2-D run at different times, we see that the initial

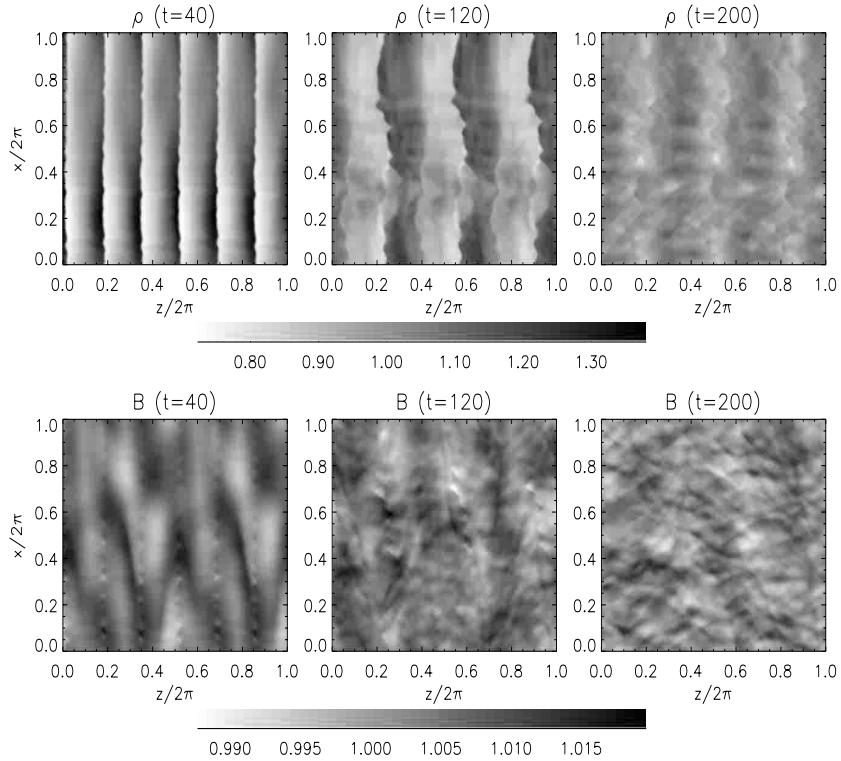

Fig. 5. Run A, 2-D case (256^2 grid points): the density (upper row) and magnetic field strength (lower row) in physical space at four different times. The train of forward propagating shocks is apparent in the first plot, where an oblique magnetosonic wave component with $\boldsymbol{k}_{c\perp} = 1$ may be recognized. In the parallel direction we see the inverse cascade $\boldsymbol{k}_{cz} = 6 \rightarrow 3$ after the secondary decay

instability occurs mainly along the average field, while the translational symmetry in the perpendicular direction is macroscopically broken only much later, during the development of the secondary decay. In Fig. 5 snapshots with isocontours of density and of magnetic field strength are shown for run A. The slow magnetosonic shock fronts are initially parallel to B_0 with a modulation in the perpendicular direction which grows in time. The inverse cascade of the excited compressive modes (secondary instability) is also apparent, the $k_z = 6$ mode being excited after the first instability and $k_z = 3$ mode after the second instability. The transverse modulation is best seen in the plots of run B, where already at $t = 40$ oblique structures have formed.

A more quantitative evaluation of the spatial properties of the evolution may be obtained by constructing 2-D reduced spectra in the $(k_z, k_\perp)$ plane. Spectral anisotropies were searched by measuring the angles between the typical energy-containing wave number in the two directions:

$$\tan^2\theta = \sum_{\boldsymbol{k}} k_\perp^2 E(k_z, k_\perp) / \sum_{\boldsymbol{k}} k_z^2 E(k_z, k_\perp). \tag{5}$$

Here $E(k_z, k_\perp)$ is the power spectrum of any Fourier-decomposable field. In three dimensions this is given by

$$E(k_z, k_\perp) = \int_0^{2\pi} E(k_\perp \cos\phi, k_\perp \sin\phi, k_z) k_\perp \mathrm{d}\phi, \tag{6}$$

easily computable numerically by summing all contributions with $k_{i-1/2}^2 < k_x^2 + k_y^2 < k_{i+1/2}^2$, where the index i is associated with the perpendicular direction. In the two-dimensional case these expressions just reduce to the sum of two elements, the pairs with opposite k_x values. Moreover, since we are dealing with power spectra of real quantities, we are allowed to use just the positive $k_z > 0$ part of it because for any second order moment the relation $E(-k_z, k_\perp) = E(k_z, k_\perp)$ holds.

In Fig. 6 the power spectra are shown, at the same times and for the same quantities as in Fig. 5, now respectively in the 2-D and 3-D cases. The calculated anisotropy angles are also reported. The overall evolution is clearly dominated by the parametric decay, in which the harmonics that are generated are well discernible even after the secondary decay. At the same time, mode couplings develop in the transverse direction in a more continuous way, so that the spectra take the shape of bands in k space. The bands of harmonics are initially limited across the magnetic field, associated with a strong anisotropy along the longitudinal direction (small θ angles) where most of the wave interaction is taking place. At longer times, they gradually fill in the transverse directions when the density spectrum approaches isotropy ($\theta \approx 45^0$), while the magnetic field spectrum shows a slight anisotropy in the perpendicular direction ($\theta > 45^0$). This situation is similar to that found by Ghosh & Goldstein (1994) in 2-D and is reminiscent of the final state assumed by an initial

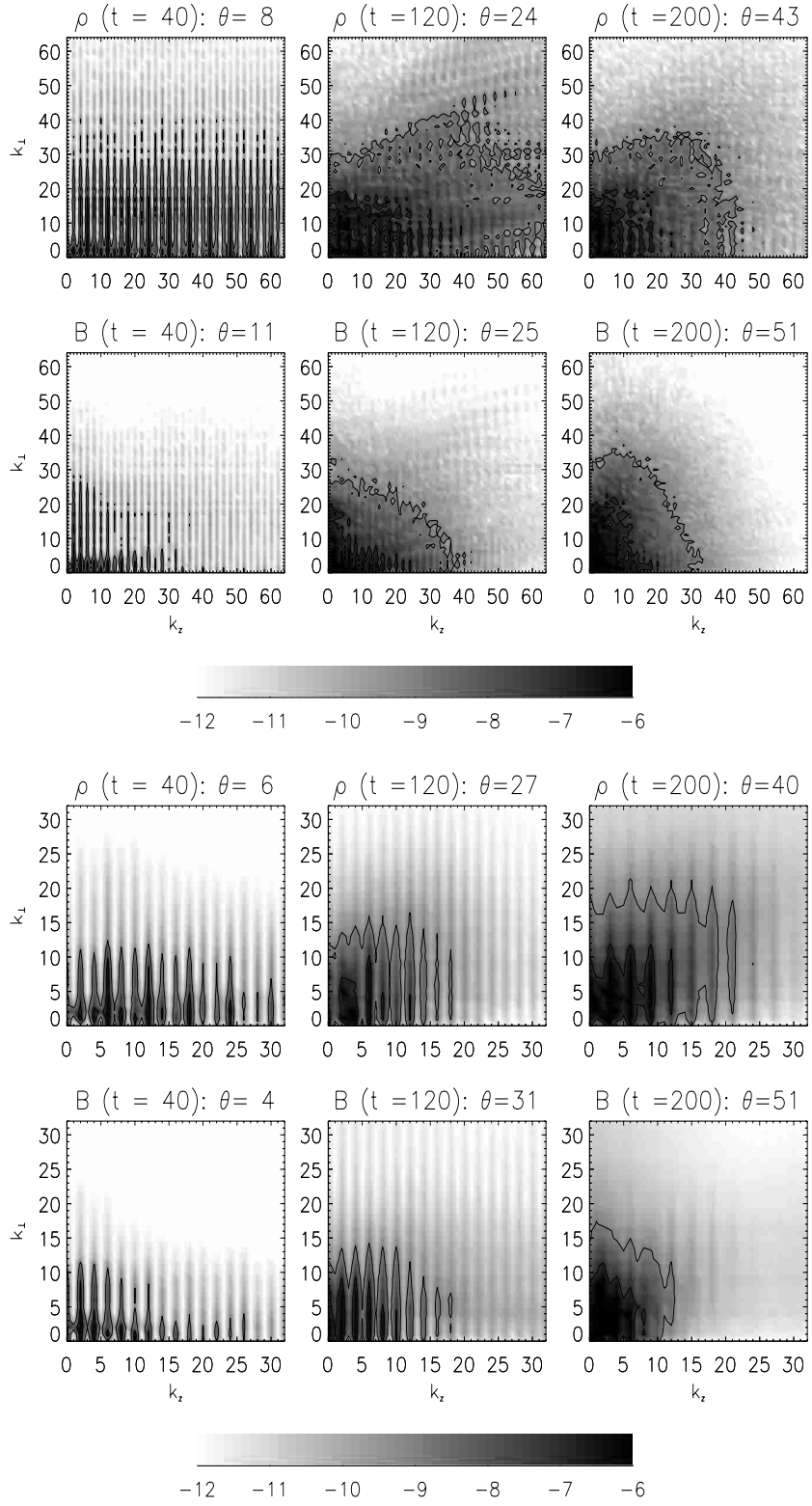

Fig. 6. Run A, 2-D case (256^2 grid points, upper plots) and 3-D case (64^3 grid points, lower plots): spectra in the $(k_z, k_\perp)$ plane for the density (upper rows) and magnetic field strength (lower rows) at the same times as in Fig. 5. The anisotropy angles are also shown, calculated according to Eq. (5)

isotropic set of fluctuations in both early incompressible MHD studies (Shebalin et al. 1982) and in more recent 3-D works in a compressible plasma (Matthaeus et al. 1996).

A higher resolution 3-D run (128^3) was also computed up to the first nonlinear saturation. In Fig. 7 the power spectra (auto-correlations) of ρ, $\boldsymbol{v}$ and $\boldsymbol{B}$ are plotted by

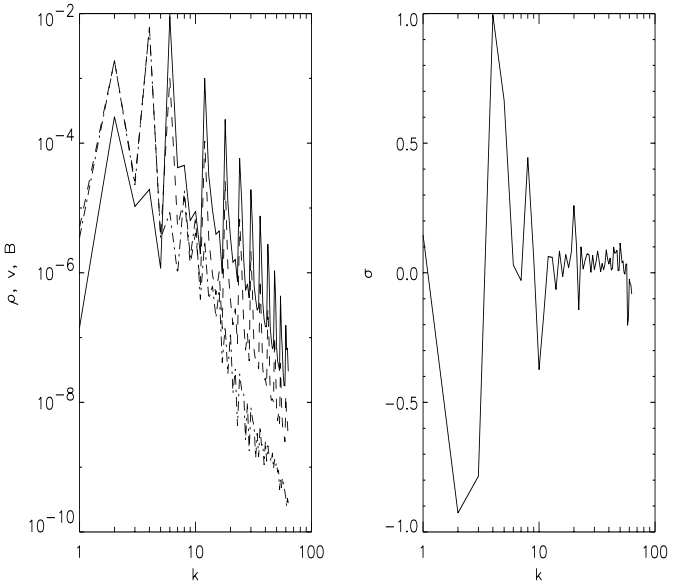

Fig. 7. Run A, 3-D case (128^3 grid points). On the left-hand side panel we show the power spectra, as a function of $k = |\boldsymbol{k}|$, of the density (solid line), velocity (dashed line) and magnetic field (dot-dashed line). On the left-hand side we plot the cross helicity, indicating strong velocity-magnetic field correlations and anti-correlations only at low wave numbers

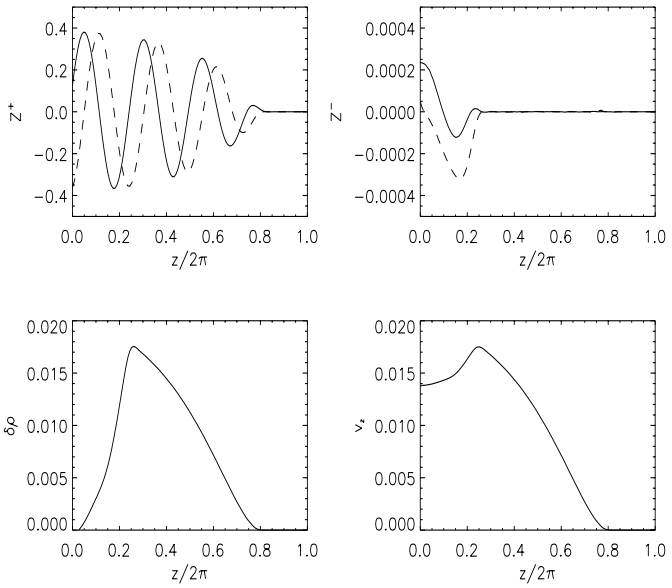

Fig. 8. Run A, 1-D case (128 grid points), $t = 5$. The Alfvén wave is injected from the $z = 0$ left hand side boundary following the function of time $(1 - \exp(-t/T_0))$, where $T_0 = 2\pi/\omega_0$ is the pump wave period. Note the creation of a (small) Alfvén wave $\boldsymbol{z}^-$ propagating in the positive direction, due to the forcing and reflected by the increasing magnetic pressure. Solid (dashed) lines in the two upper plots indicate x (y) components of the indicated Alfvén wave

reducing the original 2-D spectra to unidirectional ones in k-space. The initial pump wave has already decayed into a compressive wave with $k_c = 6$ and in the backscattered Alfvén wave with wave number $k_t^- = 2$, the latter being the new dominant mode. At this stage, the spectrum is still dominated by isolated peaks corresponding to the high order harmonics of the parametric instability. Note how the high frequency region is dominated by the compressible shocks, while Alfvénic correlation is strong only for the energy containing wave numbers. This is confirmed by the spectrum of the cross helicity, shown on the right-hand side, which has strong peaks of both sign for low k's and approaches zero for higher wave numbers.

6. Steady injection and open boundaries

All previous numerical simulations concerning parametric instability make use of periodic domains, thus one may wonder whether such process may be effective only when waves are able to interact for several periods. The only test simulation of decay of Alfvén waves in a finite domain, where the mother wave is steadily injected from one side and is able to exit freely from the other, is given in Pruneti & Velli (1997). In such work it was shown that parametric decay is robust, in the sense that it occurs on time-scales comparable to those in the periodic case, in spite of finite crossing times. This remains true even in the presence of mild gravity stratification along the mean magnetic field. In the transverse direction, a 2-D simulation showed density modulations characterized by an anti-correlation between kinetic and magnetic pressure.

Here we further investigate the multidimensional evolution of parametric decay in a numerical box with open boundaries, both in 2-D and 3-D. The initial situation is a static magnetized plasma with $\beta = 0.1$ (run A). For $t > 0$ a circularly polarized Alfvén wave with $\eta = 0.2$ and $k_0 = 4$ propagating along the mean field is gradually injected from the boundary $z = 0$. This is achieved through a variable decomposition into projected characteristics: those whose eigenvalue is positive (incoming waves) can be freely imposed (a combination of Alfvén and fast waves is needed to create a wave with $B_\perp^2 \neq 0$), while those with negative eigenvalues are left unchanged. At $z = 2\pi$ the situation is reversed but no waves are injected, so that incoming characteristics are set to zero (free outflow boundary conditions). See the Appendix for further details.

The injection of $\boldsymbol{z}^+$ in an initially homogeneous medium (with the usual density fluctuations needed to trigger the instability in the transverse directions) can be followed in Fig. 8. The incoming wave produces an initial inflow of matter and a magnetic piston, which drives a small $\boldsymbol{z}^-$ wave propagating in the positive direction. After the wave has entered, the density tends to go back to its initial value.

In Fig. 9 gray-scale plots of density distribution for a 2-D 128^2 run are shown for four different times. Note that at $t = 40$ the usual train of slow shocks have already formed, thus the instability time-scales are the same as in the periodic case, although spacing between fronts is seen to decrease with distance from the source. After $t = 40$ the fronts begin to suffer modulation in the transverse x

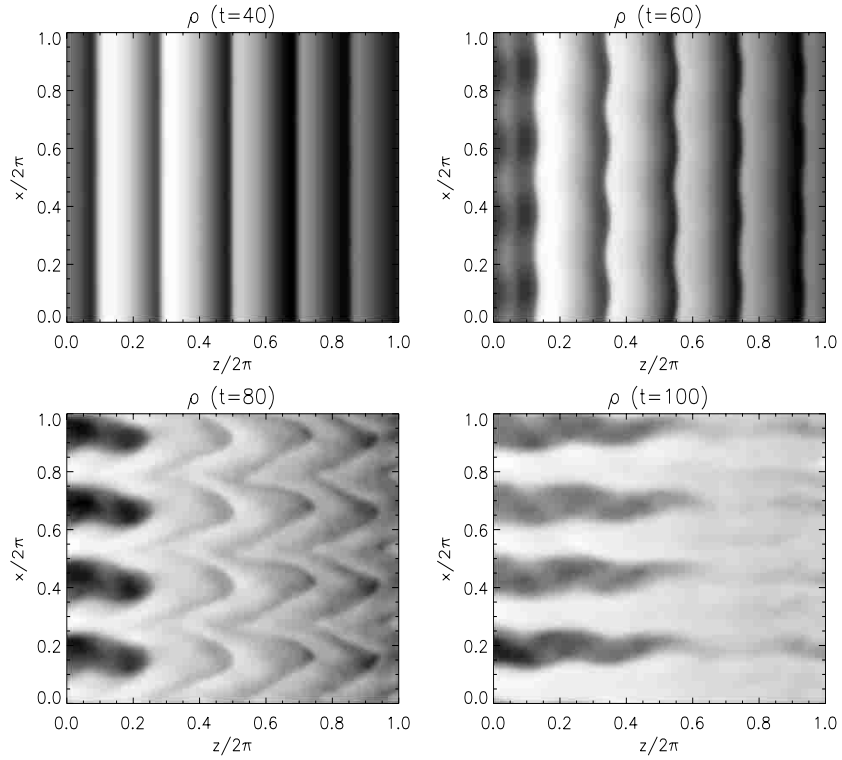

Fig. 9. Run A, 2-D case (128^2 grid points). Time series of density gray-scale plots: after the usual parametric instability, the presence of initial transverse density fluctuations triggers strong 2-D dynamics, resulting in a front modulation and a final filamentation

direction, finally leading to a situation of strong filamentation as can be seen at $t = 100$. This situation is reminiscent of density filaments identified in the extended solar corona via radio sounding measurements (Woo & Habbal 1997) and of polar plumes extending as pressure-balanced structures in the fast solar wind (Del Zanna et al. 1997; Casalbuoni et al. 1999, and references therein), although further investigations in the parameter range is of course mandatory. However, we have verified that indeed there is a growing anti-correlation of kinetic and magnetic pressure fluctuations as the time goes on. The quantity

$$\sigma_{\rm km} = \frac{< \delta p \delta p_{\rm m} >}{\sqrt{< \delta p^2 >}\sqrt{< \delta p_{\rm m}^2 >}} \tag{7}$$

takes values -0.04, 0.08, -0.30, and -0.71 at the times indicated in Fig. 9, thus the asymptotic state is one of strong anti-correlation, although an overall pressure balance is not achieved.

Slices at $z = 0$ are shown in Fig. 10 for a 3-D run. Initially the situation is rather uniform, but after $t \simeq 50$ the transverse modulation is well visible as 2-D patterns of density isocontours that progressively increase their contrast against the mean density. The large variations seen at long times are a physical consequence of the transverse coupling mentioned above; they occur because nothing, in the non-reflecting boundary conditions based on projected characteristics, prevents their growth. To conclude, we show in Fig. 11 the averaged cross helicity and Alfvénic energies at the two boundaries as a function of time, for the same 3-D run. Note the decrease of σ around $t = 30$ at the injection boundary, when the reflected wave begins to propagate backwards and exit the domain, and the final state of again purely incoming waves. The fact that E^+ increases beyond the expected maximum value $2\eta^2$ is a consequence of not having a constant density $\rho = 1$ at $z = 0$. At the upper boundary $z = 2\pi$ reflected waves are always almost negligible, so that $\sigma = +1$ from $t = 2\pi$ onwards (the time required for the injected wave to reach the opposite boundary).

7. Conclusions

The propagation of large-amplitude Alfvén waves in a magnetized uniform plasma has been studied via numerical simulations, by making use of a new high order upwind 3D-MHD code developed by the authors (Londrillo & Del Zanna 2000). Such waves are subject to parametric instability (triggered by an initial random compressive white noise) that produces daughter magnetoacoustic waves and backscattered Alfvénic modes for various values of the pump wave amplitude and plasma beta. Here we have restricted our analysis to monochromatic and circularly polarized waves in parallel propagation. The novel features introduced in our study are the extension of the simulation domain from 1-D up to full 3-D, the use of a code specially designed to treat both wave or turbulent motion and flow discontinuities (occurring all together when the instability saturates), and finally the use of simulation

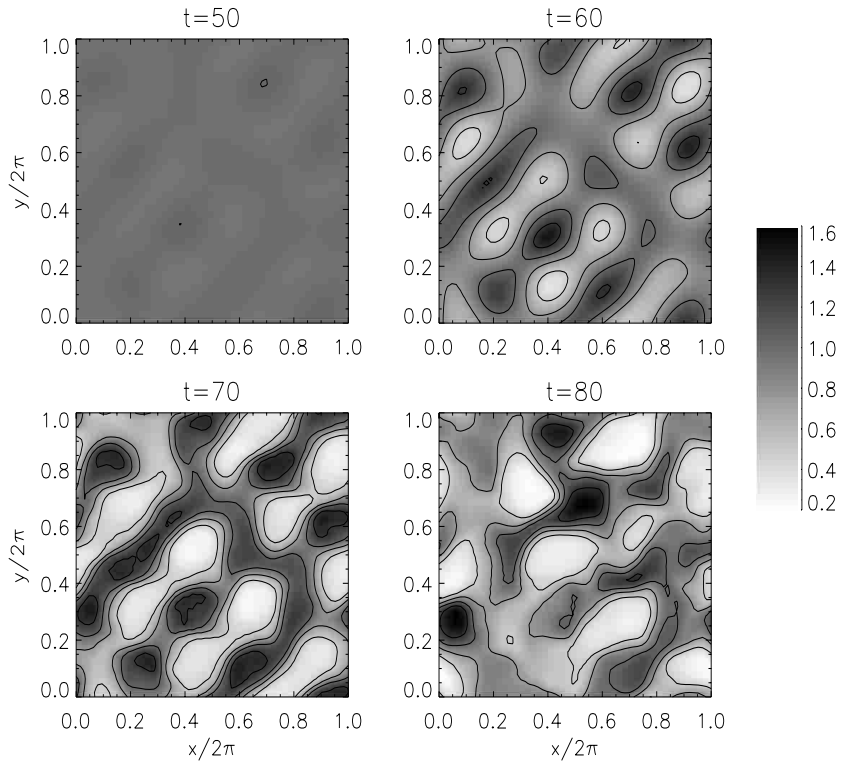

Fig. 10. Run A, 3-D case (64^3 grid points). Slices at the injection boundary ($z = 0$), at four different times, for the density. Note the very large variations induced by the pumping at long times

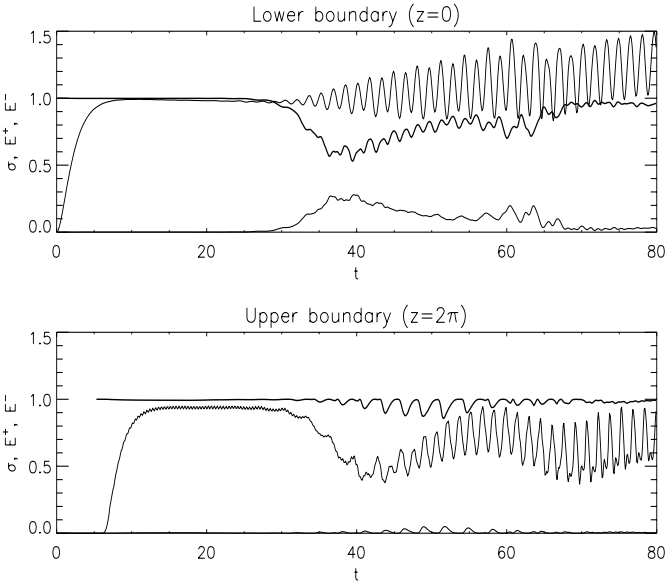

Fig. 11. Run A, 3-D case (64^3 grid points). Averaged quantities in the transverse directions at the two boundaries. Cross helicity is indicated with thick lines, while normal lines are the Alfvénic energies $E^{\pm}$ normalized against their maximum expected value $2\eta^2$

domains with open boundaries along the direction of the background field (only for the runs of Sect. 6), where the pump wave is steadily injected from one side.

Our contribution to the understanding of the parametric decay process may be summarized as follows:

- After the linear growth, the instability appears to saturate always when the generated compressive mode has steepened into a train of shocks. Discontinuous profiles in the magnetic field components also develop and these are anti-correlated with kinetic pressure fluctuations;
- The asymptotic value of the cross helicity strongly depends on the plasma beta: when $\beta \simeq 1$, corresponding to solar wind conditions, σ tends towards zero with increasing time, reminiscent of the decrease of the cross helicity with increasing heliocentric distance observed in solar wind data. However, the sign after the instability saturation appears to be well correlated with β: when it is less than one σ reverses its sign, whereas this does not hold for $\beta > 1$;
- In the low-β case we have shown, for the first time in numerical simulations, the occurrence of secondary instabilities after the first decay. In this inverse cascade the energy of the mother wave drops to zero at saturation and cross helicity reverses completely, flipping between $\sigma = +1$ and $\sigma = -1$ at each saturation step. Moreover, the total energy in the Alfvénic modes reduces approximately of a factor two at each occurrence of the instability;
- Parametric decay is essentially a one-dimensional process: in 2-D and 3-D the longitudinal behavior is practically identical, although a slight delay in the occurrence of the instability is seen, due to the

higher number of degrees of freedom in the system. Transverse modes grow with time and a final state of isotropic compressive turbulence is achieved, with a slight anisotropy in the transverse direction for quantities like the magnetic field as predicted by previous incompressible studies;
- The instability takes place with open boundary conditions too. The wave is steadily injected from $z = 0$ along the main magnetic field and fluctuations are let free to escape from the boundaries, thanks to the use of transparent characteristics-based conditions. In this case the transverse evolution is enhanced and interesting phenomena of density filamentation along the main magnetic field are observed, reminiscent of plumes in coronal holes and pressure-balanced structures in the solar wind;
- A significant anti-correlation between kinetic and magnetic pressure is always observed, even in the open-boundary case, although total pressure balance is never achieved.

Final comments are due in order to discuss in detail our assumptions (monochromatic modes, parallel propagation, circular polarization), the different results obtained in the cases of periodic and open boundaries and the possible applications of our results to open problems in solar and heliospheric physics.

When the subject of a systematic investigation is a plasma instability, it is necessary to have an initial equilibrium state, that in our case is represented by a uniform background plasma modified by the presence of a large-amplitude propagating MHD wave. Our assumptions easily ensure that the total magnetic strength is uniform, so that no ponderomotive force arises and the traveling wave remains an exact (though unstable) solution of the MHD equations at all times. Parametric instability has been shown (see the introduction) to occur also for non-monochromatic waves, so our assumption is not too restrictive in this sense. What remains to be investigated is whether waves in oblique propagation are also unstable or not. Notice that an exact large-amplitude wave with constant magnetic field strength in oblique propagation is no longer a circularly polarized wave, but is the nonlinear extension of a linearly polarized wave (arc-polarized Alfvén wave, see Barnes & Hollweg 1974). We have run a preliminary simulation with such wave as an initial condition (same parameters of run A and an angle of propagation of 30°) and we have found that it still suffers parametric decay. What is more surprising, the behavior of the characteristic quantities looks remarkably similar to that in the top panels of Fig. 2, including the occurrence of the secondary instability. This is yet another hint that parametric decay is a very general process involving nonlinear waves propagating in a compressible medium, regardless of the particular conditions of propagation direction and polarization. A comprehensive study of this more general case will be presented in a forthcoming paper.

When open boundaries are employed, though the situation is more realistic in that a wave is not forced to return periodically in the same positions and there is no restriction of having integer wave numbers, we have the problem that a portion of a traveling wave train can be followed only for a very short time, since the simulation domain is limited (2π as in the periodic runs in our specific case). Our simulations thus show what happens only very near the injection source, where the instability occurs at initial times but then is suppressed (see the time history of the cross correlation in Fig. 11) when the 2-D filamentation takes over. This process may grow just because the pump wave has always a large amplitude, while this is impossible in the periodic simulations. We conjecture here that if we could follow a wave packet for a very long time (comparable to the final times of our periodic runs) in a simulation box extending indefinitely, very similar results would be found.

The physical processes described in this paper are relevant whenever large-amplitude waves propagate in a magnetized medium. In the solar corona, where circularly polarized waves could be created by vortex-like motions at the solar surface (e.g. the *tornadoes* observed by CDS/SOHO instrument in the transition region, see Pike & Mason 1998 for the data and Velli & Liewer 1999 for a physical discussion), this mechanism could help to start a cascade towards the small scales required for dissipation, that will be presumably of kinetic nature (e.g. ion-cyclotron resonant damping). Moreover, even assuming a spatially uniform pumping of Alfvén waves from the coronal base, a process such that described in the previous section could provide an explanation for the ubiquitous density filamentation observed along the coronal fieldlines (closed loops and arcades or plumes in open field regions). However, the plasma parameters considered here are more appropriate for solar wind conditions. There the process of parametric decay could be important in shaping the MHD turbulent spectra observed in the polar regions (characterized by a rather uniform background with unidirectional mean field), where a slow but significant decrease of the cross helicity with heliocentric distance has been directly measured from data taken in situ. Our simulations clearly show that for solar wind conditions, say $\beta \sim 1$ and $B_\perp \geq B_0$, asymptotic values for $\delta\rho/\rho$ and σ are respectively about 10% and zero (in the periodic box case), as indeed observed in the data at large heliocentric distances. Finally, parametric decay could also be relevant for the evolution of the turbulence observed in molecular clouds, where the presence of large-amplitude Alfvénic waves has been invoked to drive compressive motions that can easily dissipate (see for example the final discussion in Stone et al. 1998), thus allowing to reduce the estimates of the time-scales for cloud collapse and consequent triggering of star formation activity, that is one of the most important issues in modern astrophysics.

Acknowledgements. The authors thank R. Grappin and F. Malara for fruitful discussions. Computer simulations were

performed on the Cray T3E at CINECA (Casalecchio di Reno, Bologna), under a contract CNAA.

Appendix A: Characteristics-based transparent boundary conditions

In this appendix the implementation of inflow/outflow boundary conditions will be discussed in detail, since it is an important feature of our MHD code and it has been extensively used in Sect. 6. The theory of transparent boundary conditions based on projected characteristic decomposition for hyperbolic equations is discussed in general terms by Thompson (1987), Vanajakshi et al. (1989), and Poinsot & Lele (1992); applications to solar wind problems may be found in Einaudi et al. (2000) and Grappin et al. (2000). The MHD equations may be written in vectorial form as

$$\frac{\partial V}{\partial t} + A\frac{\partial V}{\partial z} + C = 0, \tag{A.1}$$

where $V = (\rho, v_x, v_y, v_z, p, B_x, B_y)^T$. Here the z dependence has been singled out and we include in C transverse derivatives (2-D and 3-D cases) and source or geometrical terms (absent in our study). Because of the solenoidal constraint, B_z does not appear in this projected equations scheme and A is therefore a 7×7 matrix. Spectral decomposition leads to $A = R\Lambda L$ ($RL = LR = I$), in which R and L are 7×7 matrices of nonsingular normalized right and left eigenvectors and Λ is the diagonal matrix of the 7 MHD eigenvalues, usually given in increasing order, which are $\lambda^{\pm}_{\rm f,s} = v_z \pm v_{\rm f,s}$ for magnetoacoustic modes, $\lambda^{\pm}_{\rm A} = v_z \pm v_{\rm A}$ for Alfvénic modes, and $\lambda_0 = v_z$ for the entropy mode. The three characteristic velocity components along z are given by $v^2_{\rm f,s} = (1/2)\{c^2+b^2 \pm [(c^2+b^2)^2 - 4c^2b_z^2]^{1/2}\}$ and $v^2_{\rm A} = b_z^2$, with $v_{\rm s} \le v_{\rm A} \le v_{\rm f}$, where $\boldsymbol{b} = \boldsymbol{B}/\sqrt{\rho}$ and $c^2 = \gamma p/\rho$ is square of the sound speed. Note that for $b_\perp = (b_x^2 + b_y^2)^{1/2} = 0 \Rightarrow b^2 = b_z^2$ we have $v_{\rm s} = \min(c,\ v_{\rm A})$ and $v_{\rm f} = \max(c,\ v_{\rm A})$. The MHD Eq. (A.1) may be cast in the following projected characteristics form

$$L\frac{\partial V}{\partial t} + \mathcal{L} + LC = 0; \quad \mathcal{L} = LA\frac{\partial V}{\partial z} = \Lambda L\frac{\partial V}{\partial z}, \tag{A.2}$$

that, for constant A and C and by defining the Riemann invariants through $\mathrm{d}\psi_i = l_i(\mathrm{d}V + C\mathrm{d}t)$, simply reduces to $\partial_{\rm t}\psi_i + \lambda_i\partial_z\psi_i = 0$, where l_i is the left eigenvector corresponding to the eigenvalue λ_i. At the two boundaries $z = z_{\min}$ and $z = z_{\max}$ (in our case 0 and 2π, respectively), a distinction among *incoming* and *outgoing* characteristic waves has to be made, depending on the sign of the corresponding eigenvalue. For waves leaving the domain we simply define

$$\mathcal{L}_i^{\rm out} = \lambda_i l_i \left(\frac{\partial V}{\partial z}\right)_{\rm int}, \tag{A.3}$$

with spatial derivatives calculated by using interior points alone (one-sided derivatives), whereas $\mathcal{L}_i$ may be freely specified for incoming waves. If no equilibrium gradients and source terms are to be imposed, the condition $\mathcal{L}_i = 0$ for incoming waves simply allows wave propagation outside the domain without spurious reflections (transparent boundary conditions). Whatever the choice for the incoming waves, once the $\mathcal{L}_i$ have been modified the equations to solve at the two boundaries become $\partial_{\rm t}V + R\mathcal{L} + C = 0$. When the conservative variables are used, like in our upwind code, the situation is slightly different. The MHD equations in conservative form may be written as

$$\frac{\partial U}{\partial t} + \frac{\partial F}{\partial z} + H = 0, \tag{A.4}$$

where $U = (\rho, q_x, q_y, q_z, e, B_x, B_y)^T$, with $\boldsymbol{q} = \rho\boldsymbol{v}$ and $e = p/(\gamma-1) + (1/2)(\rho v^2 + B^2)$. Now, by defining $P = \partial U/\partial V \Rightarrow \partial_z F = PA\partial_z V$, $H = PC$, we have to solve the equation $\partial_{\rm t}U + PR\mathcal{L} + H = 0$ at the boundaries, with

$$\mathcal{L}_i^{\rm out} = l_i P^{-1}\left(\frac{\partial F}{\partial z}\right)_{\rm int}, \tag{A.5}$$

while incoming waves are still free.

Let us now write explicitly the right eigenvector decomposition (using the concise forms $\mathcal{M}_i = \mathcal{L}_i^+ + \mathcal{L}_i^-$ and $\mathcal{N}_i = \mathcal{L}_i^+ - \mathcal{L}_i^-$)

$$R\mathcal{L} = \begin{pmatrix} \rho(\alpha_{\rm f}\mathcal{M}_{\rm f} + \alpha_{\rm s}\mathcal{M}_{\rm s}) + \mathcal{L}_0 \\ \sigma\beta_x(\alpha_{\rm f}v_{\rm f}\mathcal{N}_{\rm s} - \alpha_{\rm s}v_{\rm s}\mathcal{N}_{\rm f}) + \beta_y\mathcal{N}_{\rm A} \\ \sigma\beta_y(\alpha_{\rm f}v_{\rm f}\mathcal{N}_{\rm s} - \alpha_{\rm s}v_{\rm s}\mathcal{N}_{\rm f}) - \beta_x\mathcal{N}_{\rm A} \\ \alpha_{\rm f}v_{\rm f}\mathcal{N}_{\rm f} + \alpha_{\rm s}v_{\rm s}\mathcal{N}_{\rm s} \\ \rho c^2(\alpha_{\rm f}\mathcal{M}_{\rm f} + \alpha_{\rm s}\mathcal{M}_{\rm s}) \\ \sqrt{\rho}[c\beta_x(\alpha_{\rm s}\mathcal{M}_{\rm f} - \alpha_{\rm f}\mathcal{M}_{\rm s}) - \sigma\beta_y\mathcal{M}_{\rm A}] \\ \sqrt{\rho}[c\beta_y(\alpha_{\rm s}\mathcal{M}_{\rm f} - \alpha_{\rm f}\mathcal{M}_{\rm s}) + \sigma\beta_x\mathcal{M}_{\rm A}] \end{pmatrix}, \tag{A.6}$$

needed once the outgoing waves have been computed with Eq. (A.5) and the incoming ones have been imposed. Here the same normalization as in Roe & Balsara (1996) has been employed, where $\sigma = \mathrm{sign}(B_z)$, $\beta_x = B_x/B_\perp$, $\beta_y = B_y/B_\perp$ ($\beta_x = \beta_y = 1/\sqrt{2}$ when $B_\perp = 0$), $\alpha_{\rm s} = [(v_{\rm f}^2 - c^2)/(v_{\rm f}^2 - v_{\rm s}^2)]^{1/2}$, $\alpha_{\rm f} = [(c^2 - v_{\rm s}^2)/(v_{\rm f}^2 - v_{\rm s}^2)]^{1/2}$ ($\alpha_{\rm s} = \alpha_{\rm f} = 1/\sqrt{2}$ when $v_{\rm f} = v_{\rm A} = v_{\rm s} = c$), with the useful relations $\beta_x^2 + \beta_y^2 = 1$, $\alpha_{\rm s}^2 + \alpha_{\rm f}^2 = 1$, $\alpha_{\rm s}^2 v_{\rm s}^2 + \alpha_{\rm f}^2 v_{\rm f}^2 = c^2$, and $\alpha_{\rm s}\alpha_{\rm f}(v_{\rm f}^2 - v_{\rm s}^2) = cb_\perp$.

In order to impose physical variables at one boundary without reflecting back outgoing waves, a number of relations in Eq. (A.6) (with $R\mathcal{L} = -\partial_{\rm t}V - C$) corresponding to the number of incoming characteristics can be inverted to yield $\mathcal{L}_i^{\rm in}$. In our specific case, while for $z = z_{\max}$ we just impose transparent boundary conditions by letting $\mathcal{L}_i^{\rm in} = 0$ when $\lambda_i < 0$, at $z = z_{\min}$ a circularly polarized Alfvén wave must be gradually injected along the positive z direction. To do so, we would like to impose

$$\boldsymbol{B}_\perp(t) = \eta B_0 f(t/\tau)(\cos\omega_0 t, -\sin\omega_0 t), \tag{A.7}$$

with, for example, $f(\xi) = 1 - \mathrm{e}^{-\xi}$, that goes asymptotically towards unity with vanishing derivative for $t \gg \tau$. Since the total magnetic pressure has to increase by a factor η^2 from the initial value $B_0^2/2$, the two magnetosonic characteristics have to be turned on too, because the Alfvénic

one alone cannot do the job. By inverting the last three relations in Eq. (A.6) we can see that the conditions

$$\mathcal{L}_{\rm A}^{\rm in} = -\frac{\sigma}{\sqrt{\rho}}(\beta_x \dot{B}_y - \beta_y \dot{B}_x), \tag{A.8}$$

$$\mathcal{L}_{\rm f,s}^{\rm in} = \mp\frac{\alpha_{\rm s,f}}{c\sqrt{\rho}}(\beta_x \dot{B}_x + \beta_y \dot{B}_y), \tag{A.9}$$

reduce automatically for $t \gg \tau$ to a pure Alfvénic pumping with $\mathcal{L}_{\rm f,s}^{\rm in} = 0$, and $\mathcal{L}_{\rm A}^{\rm in} = 2\eta k_0$ ($\omega_0 = k_0 v_{\rm A}$) when no outgoing waves are present. The results of the injection from $z = 0$, for run A parameters and with $\tau = 2\pi/\omega_0$, were shown in Fig. 8, where we can appreciate how the Alfvén wave enters smoothly the domain and the density tends to its former value after the transient phase is over.

References

Barnes, A., & Hollweg, J. V. 1974, JGR, 79, 2302
Bavassano, B., Pietropaolo, E., & Bruno, R. 2000, JGR, 105, 15959
Belcher, J. W., & Davis, L. 1971, JGR, 76, 3534
Casalbuoni, S., Del Zanna, L., Habbal, S. R., & Velli, M. 1999, JGR, 104, 9947
Cohen, R. H., & Dewar, R. L. 1974, JGR, 79, 4174
Cohen, R. H. 1975, JGR, 80, 3678
Del Zanna, L., Hood, A. W., & Longbottom, A. W. 1997, A&A, 318, 963
Del Zanna, L., & Velli, M. 2000, Adv. Space Res., to appear
Derby, N. F. 1978, ApJ, 22, 1013
Dobrowolny, M., Mangeney, A., & Veltri, P. 1980, Phys. Rev. Lett., 45, 144
Einaudi, G., Chibbaro, S., Dahlburg, R. B., & Velli, M. 2000, ApJ, to appear
Galeev, A. A., & Oraevskii, V. N. 1963, Sov. Phys. Dokl., 7, 988
Ghosh, S., Viñas, A. F., & Goldstein, M. L. 1993, JGR, 98, 15561
Ghosh, S., & Goldstein, M. L. 1994, JGR, 99, 13351
Ghosh, S., Viñas, A. F., & Goldstein, M. L. 1994, JGR, 99, 19289
Goldstein, M. L. 1978, ApJ, 219, 700
Goldstein, B. E., Neugebauer, M., & Smith, E. J. 1995, GRL, 22, 3389
Grappin, R., & Velli, M. 1996, JGR, 101, 425
Grappin, R., Leorat, J., & Buttighoffer, A. 2000, A&A, 362, 342
Hollweg, J. V. 1994, JGR, 99, 23431
Hoshino, M., & Goldstein, M. L. 1989, Phys. Fluids B, 1, 1405
Jayanti, V., & Hollweg, J. V. 1993, JGR, 98, 13247
Londrillo, P., & Del Zanna, L. 2000, ApJ, 530, 508
Londrillo, P., Del Zanna, L., & Velli, M. 2000, in Science and Supercomputing at Cineca, CINECA, Casalecchio di Reno (BO), Italy
Longtin, M., & Sunnerup, B. U. O. 1986, JGR, 91, 6816
Malara, F., Veltri, P., Chiuderi, C., & Einaudi, G. 1992, ApJ, 396, 297
Malara, F., & Velli, M. 1996, Phys. Plasmas, 3, 4427
Malara, F., Primavera, L., & Veltri, P. 2000, Phys. Plasmas, 7, 2866
Matthaeus, W. H., Ghosh, S., Oughton, S., & Roberts, D. A. 1996, JGR, 101, 7619
Pike, C. D., & Mason, H. E. 1998, Sol. Phys., 182, 333
Poinsot, T. J., & Lele, S. K. 1993, J. Comp. Phys., 101, 104
Pruneti, F., & Velli, M. 1997, in Proceedings of the Fifth SOHO Workshop: The Corona and Solar Wind near Minimum Activity, ESA SP-404, 623
Roberts, D. A., Goldstein, M. L., Klein, L. W., & Matthaeus, W. H. 1987, JGR 92, 12023
Roe, P. L., & Balsara, D. S. 1996, SIAM J. Appl. Math., 56, 55
Sagdeev, R. Z., & Galeev, A. A. 1969, Nonlinear Plasma Theory (Benjamin, New York)
Shebalin, J. V., Matthaeus, W. H., & Montgomery, D. 1983, J. Plasma Phys., 29, 525
Stone, J. M., Ostriker, E. C., & Gammie, C. S. 1998, ApJ, 508, L99
Thompson, K. W. 1987, J. Comput. Phys., 68, 1
Schmidt, J. M., & Marsch, E. 1995, Ann. Geophys., 13, 459
Umeki, H., & Terasawa, T. 1992, JGR, 97, 3113
Vanajakshi, T. C., Thomspon, K. W., & Black, D. C. 1989, J. Comput. Phys., 84, 343
Velli, M., & Liewer, P. 1999, Space Sci. Rev., 87, 339
Viñas, A. F., & Goldstein, M. L. 1991, J. Plasma Phys., 46, 107
Viñas, A. F., & Goldstein, M. L. 1991, J. Plasma Phys., 46, 129
Woo, R., & Habbal, S. R. 1997, ApJ, 474, L139
Wong, H. K., & Goldstein, M. L. 1986, JGR, 91, 5617
Zhou, Y., & Matthaeus, W. H. 1989, GRL, 16, 755